Journal of Materials Chemistry C

Accepted Manuscript

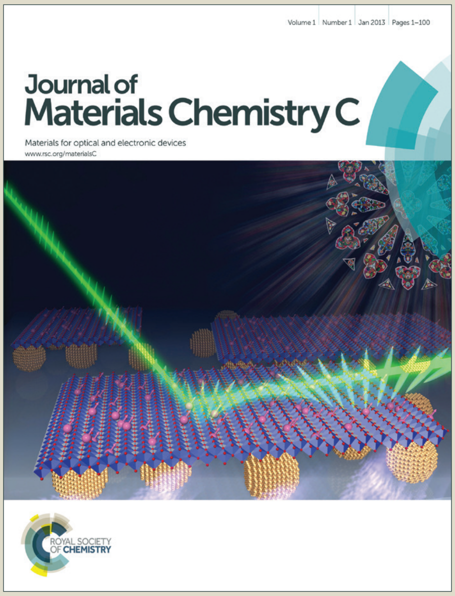

ROYAL SOCIETY OF CHEMISTRY

www.rsc.org/materialsC

Epitaxial (001) $BiFeO_3$ thin-films with excellent ferroelectric properties by chemical solution deposition-The role of gelation

Qi Zhang, Nagarajan Valanoor and Owen Standard*

School of Materials Science and Engineering, The University of New South Wales, Sydney, New South Wales 2052, Australia

*Email: o.standard@unsw.edu.au

Abstract

High quality phase pure (001) epitaxial bismuth ferrite ($BiFeO_3$; BFO) thin films have been realized by chemical solution deposition. A thorough chemical investigation of the precursor molecular changes during gelation reveals that control of the delicate balance between gelation and salt (metal nitrate) precipitation through solvent evaporation is the key to a homogenous gel, necessary to ultimately obtain high-quality films. Spin-coating at 3000 rpm for 30 seconds on a preheated STO(001) substrate (~70°C) and subsequent heating at 90°C leads to a suitable gel, which is then heated to 650°C for crystallization. Pure phase BFO thin films of 150 nm thickness prepared by this route on lanthanum strontium manganite ($La_{0.67}Sr_{0.33}MnO_3$; LSMO) buffered (001)-$SrTiO_3$ (STO) substrates are shown to have not only epitaxial nature, but also robust ferroelectric properties with low coercive field. Critically we show that these films can be achieved using stoichiometric 0.25 M precursors (with no Bi excess), thus obviating complexities typically arising from secondary phases associated with precursors having excess Bi. Square hysteresis loops with a high remanent polarization of $2P_r$ =97.8 $\mu C/cm^2$ and a low coercive field of $2E_c$=203.5 kV/cm are obtained at room temperature. Frequency-dependent hysteresis loops reveal a switching mechanism that is nucleation dominated. In addition, polarization direction dependent resistive switching behavior is also observed. The findings here thus show it is possible to realize high-quality bismuth ferrite thin films via chemical process techniques.

1. Introduction

Bismuth ferrite ($BiFeO_3$, BFO) epitaxial thin-films have been recently under extensive investigation due to their multi-functional properties[1-3]. BFO thin films show giant polarization[4, 5], polarization-mediated resistive switching[6], high piezoelectric constant[3] and unique magnetic properties[7]. Furthermore, it is innately lead-free in nature. Thus, it has significant market potential in environmentally friendly memory storage and piezoelectric devices[1, 6]. To date, the best quality epitaxial BFO thin films have been achieved generally by using physical vapor deposition (PVD) methods, such as pulsed laser deposition (PLD)[6, 8, 9] or radio-frequency (RF) sputtering[10, 11], with such films typically demonstrating high spontaneous polarization[5] and resistance switching effects[6, 12, 13].

On the other hand, the chemical solution deposition (CSD) technique is of particular industrial interest due to it being low-cost and offering accurate control of the precursor composition, as well as enabling processing ease for large-area wafers[14, 15]. In spite of these attractions, CSD-derived BFO thin films with properties comparable to PVD BFO remain a challenge. The typical difficulties associated with CSD in obtaining BFO thin films with robust ferroelectric properties include high leakage current[16-18], formation of secondary phases[18, 19], porous microstructures[15] or crystallographic defects[17]. This cannot be attributed to the chemical route or lack of appropriate precursors as indeed CSD has been successfully shown to make high quality zinc oxide (ZnO) [20] and even lead zirconate titanate (PZT) based thin films and composite structures[21]. In addition, several detailed reports have paid attention to metalorganic chemistry of such precursors and realized excellent thin films in other complex metal oxides[22, 23], and, metal-organic chemical vapor deposition (MOCVD)-derived BFO thin films (i.e. films prepared via an alternate chemical deposition technique) have shown good ferroelectric properties with square loops, high remnant polarization, and robust d_{33} values[24, 25]. Nevertheless, demonstration of CSD-derived epitaxial BFO thin films having high ferroelectric polarization or resistive switching at room-temperature has been rather elusive[26-31]. Thus far the best properties for CSD-derived BFO thin films have been reported by the Nakamura et al[28, 32]. In a series of articles they detailed phase development of polycrystalline BFO films with good P-E loops with low leakage current. Much of their discussion in terms of the frequency behavior and electric field dependence was limited to measurements performed at 80 K[32]. Unfortunately no further discussion was provided for either sol-gel processing or room temperature characterization other than that using 10% excess Bismuth yielded the best films. It is notable that only a few reports have detailed the precursor preparation and deposition processes[17, 33]. It is thus clear that understanding the chemistry of the sol-gel process is paramount to yield high quality BFO thin films.

In order to understand why this has been the case, one needs to consider the fundamental difference in phase formation pathways for thin film processes, such as PLD compared with CSD. In a typical PLD process, the deposition of the precursor (often the same stoichiometry as the end material) and the high-temperature crystallization occur nearly simultaneously. In contrast, for CSD the deposition of precursor solution onto a suitable substrate and the subsequent gelation (drying) process take place at a low temperature (<100 °C) prior to a high-temperature crystallization step[15]. Consequently the formation of a homogenous and defect-free gel film is the first critical step, with complete bearing on the final BFO thin-film microstructure, phase composition and ferroelectric properties.

Here we provide insight into the factors that govern the chemical processes during gelation (heating). In particular the delicate competition between solvent evaporation and precursor gelation, ultimately is the key factor that determines if a homogenous gel is achieved or not. Controlling this balance to yield homogenous gel films is mandatory in order to achieve epitaxial and phase-pure BFO thin films with robust ferroelectric properties.

Square P-E hysteresis loops with high remanent polarization and with very low coercive fields are obtained at a frequency range from 2 kHz to 100 kHz (i.e. $2P_r$=97.8 μC/cm^2 and $2E_c$=203.5 kV/cm at 2 kHz). Linear fitting of log(E_c) vs log(f) plot indicates a nucleation dominated domain switching mechanism for the CSD derived BFO thin films. This is supported by piezoresponse force microscopy (PFM) images which reveal a polydomain state with high domain density in these as-grown films. Local switching confirmed via PFM amplitude and phase loops reveal a coercive field $2E_c$ (~571 kV/cm) significantly larger than the global coercive field obtained via P-E hysteresis measurements. The synthesized BFO thin films also show polarization-direction dependent resistive switching behavior, in line with previous reports on PLD-obtained BFO thin films[6]. Although excess Bi is routinely added to obtain BFO films with acceptable functional properties, we show here robust properties can indeed be achieved using stoichiometric precursors provided one attains high control of the gelation process. The recipe thus eliminates any complexities that may arise from excess bismuth in the precursors.

2. Experimental Section

2.1 Precursor Preparation

Bismuth and iron nitrates, 2-methoxyethanol (2-MOE), and acetic anhydride were used to prepare BFO precursor solution for film deposition. 2-methoxyethanol (2-MOE), rather than water, was used as the solvent because of its good solubility of the various starting reagents[33] as well as it having a suitable viscosity and surface tension for spin-coating deposition[17]. Acetic anhydride, used principally as the dehydrating agent, was used here to dehydrate water of crystals from metal salt[34], as well as forming acetic acid in the precursor(see Section 3.1.2). Both dehydration and presence of acetic acid could control the extent of hydrolysis and gelation[33]. In addition, previous reports of successful perovskite thin film synthesis[33, 35, 36] point to acetic acid as an effective chelation agent. The critical role played by acetic anhydride here, in dehydrating the initial solution and to tune the solution viscosity through the formation of the oligomeric structures so as to control film morphology, will be discussed later.

BFO precursors was prepared by first dissolving bismuth nitrate ($Bi(NO_3)_3{\bullet}5H_2O$, ACS 98%, Alfa Aesar, UK) with iron nitrate ($Fe(NO_3)_3{\bullet}9H_2O$, ACS 98%, Alfa Aesar, UK) in 2-methoxyethanol (2-MOE, ACS 99.3+%, Alfa Aesar, UK) under constant stirring. Then acetic anhydride (ACS 97+%, Alfa Aesar, UK) was added to this solution under constant stirring. The molar ratio of Bi to Fe was made to 1:1 in the precursors initially. The whole preparation process was performed in an ambient atmosphere at room temperature. To identify the chemical reactions that have the most influence on the gelation process, two general precursors (Precursor A and Precursor B) were prepared with and without the effect of acetic anhydride, respectively as shown in the flowchart (Figure 1). Note that Precursor A mixture in the left flowchart has a higher 2-MOE loading (compared with the one in the right flowchart) so as to keep the metal nitrate concentration constant with Precursor B, for a better comparison of gelation process. The compositions of the precursors are shown in Table 1. Although the functional properties here are ultimately reported for films made by Precursor B, Precursor A was investigated because directly using Precursor B will not allow us to unambiguously identify the role of 2-MOE vs. acetic anhydride in the gelation process.

2.2 Precursor Characterization

Fourier transform infrared spectroscopy (FTIR) (Spotlight 400, PerkinElmer, US) was used to analyze the polymeric functional groups in 0.25 M Precursors A and B and their changes during subsequent gelation. Approximately 0.1 ml of precursor solution was dropped onto a glass substrate (25 mm × 25 mm) and the substrate then inclined to cover the surface with a uniform layer of solution. The coated substrate was placed onto a hot plate heated at 90°C for a set time then FTIR analysis of the film was acquired immediately after heating. This deposition and FTIR measurement was done for separate samples for the following heating times: 0, 15, 30, 45, 60, 75, 90, 105, or 120 seconds. FTIR patterns of the individual starting materials (2-MOE, acetic anhydride, iron nitrate and bismuth nitrate) were also measured as a reference.

2.3 Gelation Film Preparation

Thin films were prepared by dropping 0.1 ml Precursor B on glass substrates (25 mm × 25 mm) and the substrates then inclined to 90° to cover the surface with a uniform layer of solution. To enable a better observation of the gel film microstructures, films prepared in this experiment were typically thicker than the subsequent depositions on $SrTiO_3$ substrates for device characterization. After deposition, films were separately heated in air in an electric oven at 50°, 60°, 70°, 80° or 90°C for 10 minutes and then taken out of the oven and allowed to dry at room temperature in air for a further 12 hours. An additional sample was dried at room temperature in air without any heat-treatment process. After identification of an appropriate gelation temperature (>70°C), another set of as-deposited films were heated at a certain temperature (70°C) for 1, 3, 10 or 20 minutes and then allowed to dry at room temperature in air for a further 12 hours. After drying, the surface morphologies of the prepared films were studied by transmission optical microscopy (E200, Nikon, Japan).

2.4 Crystallized BFO Thin Film Preparation

Two single-layer films were produced by dropping a small amount of Precursor B onto substrates of (001)-oriented $SrTiO_3$ (STO(001), Shinkosha, Japan) with or without 70°C preheating process, followed by spin coating at 3000 rpm for 30 seconds. After the deposition, the films were heated at 90°C for 1 min for gelation followed by drying at 270°C for 3 mins. The films were then sequentially heated by putting the sample into a tube furnace preheated at 450°C and 650°C and held for 30 minutes at each temperature in an oxygen atmosphere for pyrolysis and crystallization. Atomic force microscopy (AFM; Cypher, Asylum Research, US) was used to study the microstructures of the thin film surfaces. The phase composition and preferred crystallographic orientation of the resultant films were analyzed by X-ray diffraction (XRD; X'pert Materials Research Diffractometer, PANalytical, Netherlands).

2.5 Ferroelectric Properties

For samples used for ferroelectric and electrical properties measurement, a 30 nm lanthanum strontium manganite ($La_{0.67}Sr_{0.33}MnO_3$, LSMO) layer was deposited by PLD on vicinally-cut (001) STO (Shinkosha, Japan) to form the bottom electrode. Films were spin coated onto the LSMO/STO(001) substrate using 0.25 M stoichiometric precursor (precursor B with no excessive Bi) at 3000 rpm for 30 seconds, followed by drying at 90 °C for 1 minute and 270 °C for 3 minutes. After deposition and drying, the films were then sequentially heated by putting the sample into a tube furnace preheated at 450°C and 650°C and then held for 30 minutes at each temperature in an oxygen atmosphere[37]. Au/Ti (60 nm/5 nm in thickness) top electrodes were patterned on the film surface through photolithography and metal evaporation. The size of each top electrode pad was 23 µm × 23 µm. The phase composition and preferred crystallographic orientation of the resultant films were analyzed by X-ray diffraction (XRD; X'pert Materials Research Diffractometer, PANalytical, Netherlands). A commercial scanning probe microscopy (SPM; Cypher, Asylum Research, US) was used for both AFM and piezoelectric force microscopy (PFM) measurements. Conductive Ti-Ir coated silicon cantilevers (ASYELEC-01, Asylum Research, US) were used for PFM imaging, polarization switching and piezoelectric amplitude/hysteresis loop studies. Ferroelectric behaviors were acquired using a ferroelectric testing system (Radiant Technologies, US). I-V curves through Au/Ti capacitors were measured by using Keithley 2400 SourceMeter (Keithley Instruments, US).

3 Results and Discussion

As the focus of this paper is to outline the details of the materials chemistry pathway taken to form a homogenous gel that ultimately yields a high quality BFO film, much of the results and discussion here is focused on understanding this aspect.

3.1 Precursor Characteristics

3.1.1 Precursor with No Acetic Anhydride

As-Prepared Precursor

FTIR analysis of the starting precursors was done to analyze the molecular structures prior to any changes associated with subsequent heating and gelation as shown in Figure 2. The FTIR pattern of Precursor A includes the same peaks in 2-MOE plus peaks from the metal nitrates. No noticeable change of FTIR pattern of Precursor A was observed after initial mixing of the precursors. In particular, the 2-MOE peaks in the FTIR pattern of Precursor A remained unchanged, which suggest that there were no appreciable reactions between the metal nitrates and 2-MOE solvent at room temperature.

Precursor During Heating

FTIR analysis of the Precursor A (without acetic anhydride) was done to elucidate the change(s) in chemical bonding during gelation without the complicating presence of the acetic anhydride. Figure 3(a) shows the FTIR patterns of Precursor A after heating at 90°C for various times. The FTIR patterns remain qualitatively similar for the first ~45 s of heating. By ~60 s, there is a noticeable change of peaks in the ranges of 1200-950 cm^{-1}. The films after this time had a gel-like appearance and were relatively dry after heating for 90 seconds. This correlates well with the change of FTIR peaks and suggests that appreciable reaction, presumably gelation, has occurred between the starting materials.

Given that gelation is likely to involve changes primarily in the 2-MOE solvent, better elucidation of the reactions involved in the process is made by closer analysis of the peaks over the 1200-950 cm^{-1} range. As shown in Figure 3(b), the FTIR pattern of pure 2-MOE solvent is substantially the same as that of as-prepared Precursor A with both patterns having distinct peaks at 963, 1016-1017, 1060-1061, and 1119-1121 cm^{-1}. These peaks correspond to specific bonds in specific functional groups (all of which occur in 2-MOE), namely: O–H bending bond in –CH$_2$–**OH**, C–O stretch bond in general, C–O stretch bond in –CH$_2$–**C**H$_2$**–O**H, and C–O stretch bond in a generic R–O–R′ structure which in this case pertains to **–**CH$_2$–O–CH$_3$ of 2-MOE, respectively. Following heating at 90°C for 75 s, these peaks tended to either disappear or split into lower intensity peaks as follows. The peak at 1119 cm^{-1} corresponding to C-O stretch bond in R-O-R′ splits into two peaks (1087 cm^{-1} and 1111 cm^{-1}) which indicates two different structures **of CH$_3$–O–CH$_2$-** and -**CH$_2$-O-**M in the precursor (as shown in Eqn. 1**)**, each having slightly different wavenumbers for the C-O bond[38, 39]. The peak at 1060 cm^{-1}, representing a typical C-O stretch bond in –CH$_2$-**CH$_2$-OH** group[39] , disappears after heating, which further indicates the change of -CH$_2$-OH structure in 2-MOE. Further, the C–O stretch bond[39] at 1016 cm^{-1} splits into two peaks 1009 and 1031 cm^{-1} and the O–H bending bond in –CH$_2$–OH[39] at 963 cm^{-1} disappears. These changes suggest that the O-H bond of the 2-MOE has broken on heating and, most likely, the H has been replaced with another element or functional group (in this case specifically, a Bi or Fe cation as explained later in Eqns. 1. Table 2 summarizes the functional groups in 2-MOE and in Precursor A before and after heating for 75 s.

To understand if the above changes in the molecular structure of 2-MOE during heating depend on the type of metal in the nitrate, FTIR patterns were acquired for the 2-MOE starting material and gel films derived from solutions of bismuth nitrate in 2-MOE solution, iron nitrate in 2-MOE solution, and bismuth nitrate + iron nitrate in 2-MOE solution (all after heating at 90°C for 75 s). As shown in Figure 4, no structure change is observed in pure 2-MOE after heating which indicates that the 2-MOE does not decompose or otherwise react by itself during heating. The FTIR patterns of the solutions containing metal salts are similar to each other but are substantially different to the pattern of 2-MOE. This suggests that, unlike the 2-MOE, these solutions have undergone significant molecular changes during heating. The changes are similar for the Bi solution and Fe solution as well as for the Bi + Fe mixed solution. This result suggests that the Bi and Fe undergo similar reactions with the 2-MOE, which may possibly be due to the close electronegativity values of Bi (2.02) and Fe (1.83).

The similarity of the FTIR patterns of the metal nitrates + 2-MOE solutions and the specific changes in the FTIR peaks of the 2-MOE are possibly attributed to the reaction between 2-MOE and metal nitrate to form metal-2-methoxyethanoxide[17]. As explained previously, the FTIR data suggest that the H cation in OH group of the 2-MOE is replaced and, in this case, the replacement species is likely to be either a Bi or Fe cation as shown in Eqn. 1 where M = Bi or Fe:

$$M(NO_3)_3 + 3[CH_3OCH_2CH_2OH] \leftrightarrow M(\text{-O-}CH_2CH_2\text{-O-}CH_3)_3 + 3HNO_3 \qquad \text{Eqn. 1}$$

The forward reaction in Eqn.1 only occurs when HNO_3 as the by-product is removed during the reaction, this can be achieved by adding base reagent or promoting volatility or decomposition of HNO_3. Critically, little or no gel formed when the precursor coating was heated in a sealed container, indicating that the gelation was promoted by the removal (evaporation) of the HNO_3 reaction product. It is notable that the above process was carried out using a layer on the glass substrate instead of “bulk” solution, which underlines the critical role of the evaporation rate required for forward reaction of Eqn.1 to go to completion. The boiling point of pure nitric acid is ~ 83°C at an ambient pressure and the decomposition temperature of liquid phase nitric acid is ~54°-90°C[40]. These temperatures agree well with the onset temperature (~70°C) of gelation (as discussed later in section 3.2.1). Concurrently, the large amount of excess 2-MOE in the precursor (as indicated in Table 1) drives the forward reaction in Eqn.1 and thus metal-2-methoxyethanoxide is formed.

Thus, from this section, it is found that the precursor remains as a solution of metal nitrates in 2-MOE before heating, whereas the 2-methoxyethanoxide is formed during heating (gelation) when the reactions between metal nitrates and 2-MOE occur.

3.1.2 Precursor with acetic anhydride

As-Prepared Precursor

The FTIR pattern of Precursor B (iron nitrate, bismuth nitrate, 2-MOE and acetic anhydride) is shown over a wave-number range of 2000-780 cm^{-1} in Figure 5 along with the patterns for 2-MOE, acetic anhydride, and Precursor A for the purposes of comparison. It is notable that whilst the FTIR patterns for 2-MOE and Precursor A are very similar to each other (indicating little by way of any chemical reactions on mixing as explained in Section 3.1.1), the FTIR pattern of Precursor B is very different to that of 2-MOE as well as to that of Precursor A. Moreover, despite there being an appreciable amount of acetic anhydride in Precursor B, most of the FTIR peaks corresponding to the former are not apparent in the FTIR pattern for Precursor B. In particular, FTIR peaks for the acetic anhydride at 1824 and 1751 cm^{-1} (corresponding to the C=O stretch bond in the $(CH_3CO)_2O$ structure[39]) disappear completely after mixing with the metal nitrates and 2-MOE to form Precursor B, while a peak at 1740 cm^{-1} (corresponding to the C=O stretch bond in ester (RCOOR′) structures[39]) and another at 1719 cm^{-1} (corresponding to the C=O stretch bond in acetic acid (CH_3COOH)[39]) emerge. These results indicate that significant chemical reactions occur during the initial mixing of Precursor B and these are considered in more detail next.

The FTIR pattern (shown in Figure S1.1) of a mixture of 2-MOE and acetic anhydride showed the FTIR peaks corresponding to these two chemicals and it is notable that the FTIR peaks of ester (at ~1730 cm^{-1}) and acetic acid (at ~1715 cm^{-1}) were absent. This indicates that no chemical reaction between 2-MOE and acetic anhydride occurred on mixing these two organic materials at room temperature. However, it should be noted that FTIR patterns revealed ester formation in the mixture after storing in a sealed container at room temperature for 1 week – this suggests that the mixture does react slowly undergoing an esterification reaction. In contrast, the addition of acetic anhydride to a solution of 2-MOE and metal nitrates resulted in a rapid rise in temperature to ~70-90°C. It is considered that this is caused by the reaction between acetic anhydride and the water of crystallization (from the metal nitrates) to form acetic acid as follows:

$$(CH_3CO)_2O + H_2O \rightarrow 2CH_3COOH \qquad \text{Eqn. 2}$$

The reaction in Eqn. 2 is exothermic and the heat produced triggers the esterification reaction between 2-MOE and acetic anhydride to form acetic acid and 2-methoxyethyl acetate as shown in Eqn. 3. It is also likely that that metals (Bi or Fe from the starting nitrates) act as catalysts for Eqn. 3[41] .

$$(CH_3CO)_2O + CH_3OCH_2CH_2OH \rightarrow CH_3COOH + CH_3OCH_2CH_2OCOCH_3 \qquad \text{Eqn. 3}$$

The lack identifiable peaks of acetic anhydride in the FTIR pattern of Precursor B (Figure 5) indicates that the acetic anhydride has been completely consumed in the reactions of Eqns. 2 and 3. Lastly, it is likely that the exothermic heat of Eqn.2 also provides heat for the reaction between the metal nitrates and 2-MOE to form metal-2-methoxyethanoxide (Eqn. 1 as discussed previously – see section 3.1.1).

The above FTIR analysis and Eqn. 1-3 show that, unlike Precursor A, chemical reactions commence immediately on mixing of the metal nitrates, 2-MOE, and acetic anhydride and that the effective starting composition of precursor B prior to deposition is actually a mixture of metal-2-methoxyethanoxide $M(CH_3OCH_2CH_2O)_3$, 2-MOE (CH_3-O-CH_2-CH_2-OH), acetic acid (CH_3COOH) and 2-methoxyethyl acetate ($CH_3COOCH_2CH_2OCH_3$). The composition of the as-prepared precursor has also been confirmed by using NMR, which is discussed in supplementary S2.

Precursor During Heating

Figure 6(a) shows the FTIR patterns of Precursor B after mixing ("starting material") and after heating at 90°C for various times up to 120 s. Like Precursor A, precursor B also showed a noticeable change in the shape of the FTIR patterns after ~60 s. Closer inspection of the 1200-950 cm^{-1} range (Figure 6(b)) shows the presence of peaks of the C-O bond in 2-MOE or 2-methoxyethyl acetate ($CH_3COOCH_2CH_2OCH_3$) in the starting precursor and after 90 s of heating. Similarly, the 1850-1650 cm^{-1} range (Figure 6(c)) shows the presence of peaks of the C=O bond in acetic acid (CH_3COOH) and ester, in this case 2-methoxyethyl acetate ($CH_3COOCH_2CH_2OCH_3$), in the starting precursor and after 90 s of heating. The FTIR peak positions of these functional groups are summarized in Table 3. The main change in the FTIR patterns on heating is the loss of the C-O bond in the -CH_2-**C**H_2-**O**H group (at 1052 cm^{-1}). This attributed to the loss of OH groups on the 2-MOE as the solvent reacts the acetic anhydride (Eqn. 3) and metal nitrates (Eqn. 1).

The formation of acetic acid in Precursor B gives a possible variation to the reaction between the metal nitrates and 2-MOE (Eqn. 1) in that some acetic acid could react with the metal nitrates[17, 42] as indicated in Eqn.4.

$$M(NO_3)_3 + x[CH_3OCH_2CH_2OH] + (3-x)CH_3COOH$$

$$\leftrightarrow M(OCH_2CH_2OCH_3)_x\,(OOCCH_3)_{3-x} + 3HNO_3 \qquad \text{where } x \leq 3 \qquad \text{Eqn. 4}$$

The FTIR data (Figure 6(c) and Table 3(b)) indicate a slight shift of the C=O peak from 1722 $\mathrm{cm^{-1}}$ to 1709 $\mathrm{cm^{-1}}$ and it is possible that this is due to the acetic acid reacting with metal nitrate[33]. Although this reaction is possible, the FTIR data do not indicate the extent of this reaction compared with Eqn. 1.

Precursor B formed an obvious visible gel after ~60 s at 90°C. Gelation is considered to be by primarily the condensation of the metal-2-methoxyethanolxide as follows:

$\mathrm{n[M(CH_3OCH_2CH_2O)_3]} \rightarrow$

$\mathrm{(CH_3OCH_2CH_2O\text{-})_2\,M\text{–}[O\text{-}M(\text{-}O\text{-}\,CH_2CH_2\text{-}O\text{-}CH_3)]_{n\text{-}2}\text{-}O\text{-}M(\text{-}O\text{-}\,CH_2CH_2\text{-}O\text{-}CH_3)_2}$

$\mathrm{+\ (n\text{-}1)[CH_3OCH_2CH_2OCH_2CH_2OCH_3]}$ Eqn. 5

Alternatively, condensation could involve $\mathrm{M(CH_3OCH_2CH_2O)_x(CH_3COO)_y}$[33], for example,

$\mathrm{n[M((\text{-}O\text{-}\,CH_2CH_2\text{-}O\text{-}CH_3)_x(OOCCH_3)_y]} \rightarrow$

$\mathrm{(CH_3OCH_2CH_2O)_x(CH_3COO)_{y\text{-}1}M\text{–}[O\text{-}M(CH_3COO)]_{n\text{-}2}\text{–}O\text{-}M(\text{-}O\text{-}\,CH_2CH_2\text{-}O\text{-}CH_3)_{x\text{-}1}\,(OOCCH_3)_y}$

$\mathrm{+\ (n\text{-}1)[CH_3COOCH_2CH_2OCH_3]}$ Eqn. 6

Denoting R as either $\mathrm{CH_3OCH_2CH_2\text{–}}$ or $\mathrm{CH_3CO\text{–}}$, Eqns. 5 and 6 may be written more simply as:

$\mathrm{n[M(OR)_3]} \rightarrow \mathrm{M(OR)_2\text{–}[OM(OR)]_{n\text{-}2}\text{–}OM(OR)_2\ +\ (n\text{-}1)ROR}$ Eqn. 7

The reaction sequence of the above process is summarized in Table 4. In the subsequent pyrolysis process (to 450°C), the organic groups of the gel will be decomposed and removed, leaving -M-O- as the final bond structure in the films. Provided that the composition is stoichiometrically correct, this oxide structure will be eventually converted to perovskite BFO during subsequent high-temperature crystallization.

The effect of acetic anhydride is evident in that the drying time of Precursor B films are much longer than those of Precursor A films under the same heating conditions. This is attributed to the formation of an ester in Precursor B which lowers the solution's vapour pressure thus decreasing the drying rate and reducing the opportunity for precipitate formation. Accordingly, the discussion in the following section (Section 3.2.2) and a comparison of film topography (see supplementary S3), confirm that Precursor B is more suitable to prepare homogenous gel films. The rest of the manuscript thus focusses on the recipe development using Precursor B.

3.2 Film Gelation

3.2.1 Effect of Gelation Heating Condition

Figures 7(a)-(f) show microstructures obtained by optical transmission light microscopy for thin films deposited on glass using 0.25 M Precursor B and heated treated for a fixed time of 10 minutes at various temperatures (RT, 50°C, 60°C, 70°C, 80°C, and 90°C) followed by drying at room temperature under conditions for a further 12 hours. Films heated at 60°C and below contain salt precipitates distributed in a transparent gel matrix. In the RT films, the precipitates show needle-like (~200-400 µm in length and ~20 µm in width) and flake-like shapes, which covers nearly 80% of the film surface area. In the 50°C films, the precipitates show a needle-like shape, which are ~50-100 µm in length and ~20 µm in width. In both the RT and 50°C films, these appear to lie in the plane of the film due to the constraint imposed by the thickness of the film. Precipitates are also present in the films heated at 60°C but these are much smaller (<10 µm) and are relatively equiaxed. The coverage of the precipitates on the film surface decreases as the increase of heating temperature. As shown in Figures 7(d)-(f), no precipitates were observed (up to the maximum magnification of 1000×) in films heated at 70°C, 80°C and 90°C with the films appearing to consist entirely of a uniform, transparent gel.

Similarly, precipitate-free gels were observed for the 0.35 M and 0.45 M precursors heated at 70°C and above (not shown here). Figures 7(g) and (h) show the microstructures for thin films deposited on glass using 0.35 M and 0.45 M precursors and heated at 60°C for 10 minutes followed by drying at room temperature for 12 hours. Compared with films derived from 0.25 M in Figure 7(c), the coverage of the precipitates on the film surface is clearly increased with the increasing metal salt concentration in the precursors. Notably, the above precipitates did not form during the heat treatment but rather formed during the subsequent 12 hours drying in air at room temperature.

On the basis of these results, a temperature of 70°C was chosen to evaluate the effect of heating time on film drying and gelation. Although we show later that temperatures higher than 70°C are appropriate for practical processing, in this section we show results using 70°C as our gelation temperature. This is because at 70°C, the rates of drying and precipitation are sufficiently slow, such that their competition can be elucidated. Heating temperatures at higher than 70°C accelerates the solvent evaporation sufficiently such that this completion between gelation and precipitation cannot be observed. Figures 8(a)-(d) show microstructures of thin films prepared by 0.25 M precursor heated at 70°C for various times (1, 3, 10, and 20 minutes) followed by drying at room temperature in ambient atmosphere for a further 12 hours. Films heated for 1 minute and 3 minutes contain needle-like (~50-100 µm in length and ~10-20 µm in width) and small granular-like precipitates (~10 µm) distributed in a transparent gel matrix, respectively. Figures 8(e) and (f) show the microstructures of thin films prepared by 0.35 M and 0.45 M precursor, respectively, heated at 70°C for 3 minutes) followed by drying at room temperature for 12 hours. Flower-like precipitates are observed from both 0.35 M and 0.45 M. Again, it was observed that these precipitates formed only during the subsequent drying stage and not during the heat treatment. Films prepared by 0.25 M, 0.35 M (not shown) and 0.45 M (not shown) heated for 10 minutes or more consisted entirely of a transparent gel and no precipitates were observed (up to the maximum magnification of 1000×). Table 5 shows the summary of the effect of gelation heating conditions (heating temperature and duration) on the thin-film microstructure.

3.2.2 Proposed Mechanism

From the above descriptions, the dried films can be classified into three distinct morphologies: transparent gel film with distinct precipitates, completely transparent gel film, and powdery film (found in thicker films, as discussed in S4) without any apparent gel. The formation of these different morphologies can be interpreted in terms of the processes of film gelation versus film drying and the contributory effects of temperature, time, and film thickness. Film gelation is considered to occur by the chemical reactions described in Section 3.1 (i.e., Equations 1-6) whereas film drying is due to the evaporation of the solvent from the film.

As discussed in Section 3.1, the bonds between metal nitrate and organic solvent have not been formed in the as-prepared precursor A. At best they are partially formed, as in case of the as-prepared precursor B. Considering the effect of temperature first, it is apparent that lower temperatures (≤ 60°C) tended to produce transparent gel films containing distinct precipitates. At these temperatures, both the evaporation rate of the solvent and the gelation rate (controlled by the rate of nitric acid removal in Eqn.1) would be expected to be relatively slow. Although gelation occurred, the rate of solvent evaporation was sufficiently fast such that the concentration of metal salts in the solvent increased significantly to reach its solubility limit whilst the film was still sufficiently fluid thus resulting in appreciable precipitation.

With increasing temperature, but significantly below the boiling point of 2-MOE (125°C), the rate of gelation would be expected to increase relative to the rate of solvent evaporation thus resulting in a greater amount of gelation prior to the onset of any precipitation. Also, the gelation process (Equations 1, 4, 5, and 6) consumes the cations thus decreasing their concentration in the remaining solvent. This counteracts the increase in cation concentration in the solvent that would otherwise occur due to solvent evaporation and thus helps to maintain the metal nitrate concentration below solution saturation so as to delay the onset of any precipitation. When precipitation does begin, its progression is less favorable because (i) there is a smaller amount of "free" cations available in the solvent for precipitation and (ii) the formation of the gel phase increases the net viscosity of the solvent-gel system resulting in slower diffusion rates of the cations and anions involved in precipitate growth. The net result is that the size and amount of precipitates formed in the gel would be expected to get smaller as the initial heating temperature increases until a temperature is reached at which gelation dominates over precipitation. The micrographs shown in Figure 7(a)-(c) agree with the above explanation in that the amount and size of the precipitates formed in the thin films (at 10 minutes) diminish as the temperature increases from RT to 50°C to 60°C, with no precipitates being apparent in the films heated at 70°C and higher. For the latter films, it is considered that the gelation reactions involving the metal nitrates and 2-MOE solvent proceed to completion (without the formation of precipitates) with the remaining excess solvent evaporating to yield the final dry transparent gel.

Explanation of the effect of time on the film morphology is not as straightforward. Counterintuitively, films treated at 70°C for 10 minutes or longer yielded transparent films without precipitates whereas heating for only 3 minutes (or less) at this temperature resulted in precipitation (Figure 8). The observation (see section 3.2.1) that the precipitates formed not during the 3 minutes at 70°C but instead during the subsequent 12 hours under ambient conditions is significant for two reasons. Firstly, holding the film at 70°C would favor gelation over precipitation as already explained for the effect of temperature. However, it is possible that holding the film at this temperature for just 3 minutes (or less) resulted in only partial gelation such that on cooling to room temperature there was still an appreciable amount of solvent left. Secondly, subsequent holding of the film under ambient conditions and the resultant growth of precipitates is in agreement with explanation of the effect of temperature. That is, at lower temperature the rate of solvent evaporation is fast relative to that of gelation such that the metal salt concentration in the film increases with drying time leading to saturation and thus precipitation. In contrast, it is apparent that holding at 70°C for 10 minutes (and longer) was sufficient for the film to gelate to such an extent to prevent any subsequent precipitation.

3.2.3 Recipe Development — Effect of Metal Nitrate Concentration in Precursor, Preheating Process and Precursor Stoichiometry

(1) Metal Nitrate Concentration in Precursor

The effect of the metal nitrate concentration in the precursor on the gelation process as shown in Figure 7 and Figure 8, and the discussion in supplementary S5 and S6 further confirm the above mechanism of gelation. As discussed in S5 and S6, the precursor with higher metal nitrate concentration has a higher vapor pressure which has a faster evaporation rate during heating than the low concentration precursors. Thus, more precipitates were formed in the 0.35 M and 0.45 M precursors than 0.25 M precursor when heating under identical conditions (as shown in Figure 7(c)(g)(h) and Figure 8(c)(e)(f)). It suffices to mention that 0.25 M of iron nitrate (and bismuth nitrate) in the precursor was identified as the optimal concentration.

(2) Preheating Process

As spin-coating process is typically used to prepare CSD derived thin-films, it is important to prevent the precipitation driven by the evaporation of precursor solvent during spinning. Thus, preheated substrates (at ~70°C) are used for spin coating deposition and this is discussed in supplementary S6 in detail. Figure 9(a)(b) shows the AFM images of thin films prepared by deposition of 0.25 M Precursor B on STO(001) substrate with or without preheating at 70°C, respectively, followed by spin coating, drying, pyrolysis and crystallization. Homogenous film topography is observed for films with preheating process, showing relatively small RMS roughness of approximately 1.9 nm. In contrast, discrete grains (with a size of ~0.5 um) distributed over the film surface are observed for the films with no preheating process and these increases the film roughness to around 8 nm. Figure 9(c) shows the XRD of the films prepared with and without preheating. Phase pure BFO thin films with only (00*l*) orientation peaks were obtained when using preheated substrates, while a bismuth-rich secondary phase and (110) BFO orientation were found in the films using substrates with no preheating. Thus, the precipitates forming during spinning and following gelation contribute to the secondary phases impurities (see EDS analysis in supplementary S7) and crystallographic defect (misorientation), which would further detriment the ferroelectric properties of BFO thin films.

(3) Initial Precursor Bi:Fe Stoichiometry

To prepare BFO thin films, Bi-excess precursor (or target) is commonly used in many deposition methods (i.e. PLD, CVD, etc) to compensate the loss of Bi during high-temperature crystallization (annealing). However, the accurate control of excess Bi in the precursor adds additional complexity. Firstly it has been shown that excess A-site loading can severely compromise the ferroelectric properties of PZT thin films analogs[43], as the excess Pb (in this case Bi) drives secondary phase formation. Although stoichiometric BFO can be produced when the Bi evaporates homogenously from the $Bi_{1+x}FeO_3$ thin films in PVD processes, for CSD films a highly uniform BFO gel film is required. According to the above investigation and discussion of gelation mechanism, any inhomogeneous composition (i.e. precipitates) in the gel film may contribute to secondary phases in final crystallized BFO thin film. This leads to not only a rough surface and/or misorientated crystals, but also significantly increased dielectric leakage. Although Nakamura et al found that 10% excess Bi was required in their CSD process to obtain films with acceptable functional properties[32], we show here that robust properties can be achieved using stoichiometric precursors provided there is good control of the gelation process.

(4) Gelation heat treatment and subsequent phase development

The films prepared using the above precursors were then spun on a preheated substrate and allowed to heat at 90°C for 1 minute for gelation. This time of 1 minute is sufficient to obtain uniform gel (See supplementary S8). The films were then subsequently heated at 270°C for 3 minutes for drying. After that, the dried films were rapidly heated to 450°C and 650°C in oxygen atmosphere for 30 minutes, sequentially to obtain the phase pure BFO thin films with epitaxial structure. The details of the phase development has been discussed in our previous report [37].

3.3 BFO Thin Film Characterization

Using above optimized precursor recipe and homogenous gel film preparation process, phase-pure BFO films of 150 nm thick were prepared on (001)-LSMO buffered STO substrates. Figure 10(a) shows the XRD pattern of as-prepared (001)-BFO/LSMO/STO thin film. BFO (00*l*) peaks are observed and no crystallographic misorientation nor secondary phase in the film. The AFM topographic scan shown in Figure 10(b) confirms a smooth surface with no open pores or cracking. Cross-section EDS analysis (shown in supplementary S7) was performed across the entire film cross section to map the A-site stoichiometry. On average, EDS analysis of the films showed that the films are deficient in bismuth. The Bi:Fe ratio varies from 43.2:56.8 to 46.5:53.5 for scans collected over 150 nm. But we also note that this deficiency does not compromise the yield of smooth gel films or eventually the ferroelectric performance. The ratios obtained here are in agreement with the reports of Sawa et al[44], who found that slightly Bi deficient films made via PLD had attractive resistive switching properties. However, it is notable that neither the physical features (such as roughness, secondary phases, etc.) nor electrical properties are severely compromised by this slight deficiency.

The PFM phase in Figure 11(a) shows domain switching behavior of BFO thin film. A 3 µm × 3 µm square region was switched first by applying a DC bias of -9 V. Subsequently, an opposite

DC bias of +9 V was applied in a square region of 1 μm × 1 μm in the center of previous 3 μm × 3 μm square region to switch the polarization back. Both the virgin-domains from the un-switched area and the regions of switched domains present a uniform domain distribution, demonstrating the homogenous phase composition of as-prepared BFO thin film, as well as its ferroelectric nature. Figure 11(b) shows the local PFM amplitude and phase hysteresis loops. A square loop indicating a sharp 180° change in PFM phase and a butterfly loop in PFM amplitude are observed, demonstrating good ferroelectric switching behavior. Coercive field $2E_c$ from the local PFM loops is approximately 571.25 kV/cm.

Critically, well saturated and square-like ferroelectric polarization loops are obtained in our CSD-derived BFO thin films measured at frequency range from 2 kHz to 100 kHz at room temperature, as shown in Figure 11(c). The remanent polarization $2P_r$ and coercive field $2E_c$ are 97.8 $\mu C/cm^2$ and 203.5 kV/cm, respectively, at 2 kHz. These ferroelectric properties are comparable with PLD-derived BFO (001)-oriented epitaxial thin films (200 nm in thickness)[3,45]. Moreover, our CSD derived BFO thin-film shows a smaller coercive field ($2E_c$ of 203.5 kV/cm) compared with typical PLD-derived counterparts (~300 kV/cm). The low coercive field of our BFO thin films is due to the high density of domain walls which facilitates the nucleation of new domains during switching. The linear fits of the $\log(E_c)$ vs $\log(f)$ plot (average of 8 measurements on different top electrodes) in Figure 11(d) obey the relationship $V_c \propto f^{\beta}$ [46], which follows the domain switching model[47] as given by Scott[48]. This indicates that the switching kinetics are influenced by domain nucleation facilitated by the large density of domain boundaries and thereby reducing the coercive field. The value of β near 30 kHz changes from 0.05 to 0.15, indicating a change in the dimensionality of the nucleus shape at that frequency. This switching mechanism is further evidenced by the value of $2E_c$ obtained by local PFM loops acquired within a single domain (where few or no domain walls are involved). Although a direct comparison is not accurate (due to the complex nature of electric field distribution under the PFM tip), the estimated value ($2E_c$ =

571.3 kV/cm) is statistically (at least 10 measurements at different points) much higher than those found for the P-E hysteresis loops ($2E_c$ = 203.5 kV/cm (at 2 kHz) to 304.3 kV/cm (at 100 kHz)).

Additionally, resistive switching behavior was observed for the BFO thin film, as seen from its current-voltage (I-V) curves in Figure 11(e). The I-V spectra were acquired by a triangular ramp voltage sweep from -9V to + 9V and back to -9V. An open loop is observed. The black curves represent the high resistive state (HRS, OFF state) and the blue are the low resistive switching state (LRS, ON state). A clear jump from the HRS to LRS is observed around the positive coercive voltage, indicating this jump is derived from polarization switching, however, the negative side is not as clear.

4. Conclusions

In summary, high-quality BFO thin films have been prepared by CSD technique. The CSD precursors were prepared by mixing the iron nitrate, bismuth nitrate, 2-methoxyethanol and acetic anhydride. FTIR spectroscopic investigations of the molecular structural change in the precursor during gelation (heating) and for varying gelation conditions revealed a competition between the solvent evaporation and precursor gelation to play a key role in preparing homogenous gel films and subsequent crystallization of high-quality BFO thin films. In particular this study shows that using a 0.25 M stoichiometric precursor, a uniform BFO gel thin film can be prepared by dropping the precursor on a 70°C preheated substrate followed by spin-coating process and subsequently heating at 90°C for gelation. Heating the uniform gel-film to 650°C in an oxygen atmosphere, yielded phase-pure 150 nm thick (001)-oriented BFO epitaxial thin on a LSMO/STO(001) substrate.

Robust ferroelectric properties with square hysteresis loops, low dielectric leakage and resistive switching for the BFO thin films were shown at room temperature. The local ferroelectric nature of BFO thin films was confirmed through PFM domain switching and local PFM amplitude and phase loops. Square-like ferroelectric polarization hysteresis loops are obtained with a high remanent polarization ($2P_r$ =97.8 μC/cm^2 at 2 kHz) and a low coercive field ($2E_c$=203.5kV/cm at 2 kHz) at a frequency range from 2 kHz to 100 kHz. Linear fitting of log(E_c) vs log(f) plot indicates a nucleation dominated domain switching mechanism for the BFO thin films. In addition, the resistive switching behavior was found in the BFO thin film as well. These findings suggest CSD as a viable low-cost deposition alternative, and thus offer an exciting potential for industrial BFO mass manufacture.

Acknowledgement

This research has been supported by the University (International) Postgraduate Award from the University of New South Wales. NV acknowledges the support from ARC Discovery and LIEF grants. The authors would like to thank Hsin-Hui Huang and Yanyu Zhou for their efforts on the TEM and EDS analysis, Australian National Fabrication Facility (ANFF, UNSW) for their lithography and metal evaporation equipment for the top electrode preparation, and Dr. Donald Thomas from Mark Wainwright Analytical Centre (UNSW) for NMR measurement.

References

[1] G. Catalan and J. F. Scott, Adv. Mater., 2009, **21**, 2463
[2] J. F. Scott, J. Mater. Chem., 2012, **22**, 4567
[3] J. Wang, J. B. Neaton, H. Zheng, V. Nagarajan, S. B. Ogale, B. Liu, D. Viehland, V. Vaithyanathan, D. G. Schlom, U. V. Waghmare, N. A. Spaldin, K. M. Rabe, M. Wuttig and R. Ramesh, Science, 2003, **299**, 1719
[4] C. Ederer and N. A. Spaldin, Phys. Rev. Lett., 2005, **95**, 257601
[5] J. X. Zhang, Q. He, M. Trassin, W. Luo, D. Yi, M. D. Rossell, P. Yu, L. You, C. H. Wang, C. Y. Kuo, J. T. Heron, Z. Hu, R. J. Zeches, H. J. Lin, A. Tanaka, C. T. Chen, L. H. Tjeng, Y. H. Chu and R. Ramesh, Phys. Rev. Lett., 2011, **107**, 147602
[6] A. Q. Jiang, C. Wang, K. J. Jin, X. B. Liu, J. F. Scott, C. S. Hwang, T. A. Tang, H. Bin Lu and G. Z. Yang, Adv. Mater., 2011, **23**, 1277
[7] C. J. Cheng, C. L. Lu, Z. H. Chen, L. You, L. Chen, J. L. Wang and T. Wu, Appl. Phys. Lett., 2011, **98**, 242502

[8] L. You, N. T. Chua, K. Yao, L. Chen and J. L. Wang, Phys. Rev. B, 2009, **80**, 024105

[9] C. Himcinschi, I. Vrejoiu, M. Friedrich, E. Nikulina, L. Ding, C. Cobet, N. Esser, M. Alexe, D. Rafaja and D. R. T. Zahn, J. Appl. Phys., 2010, **107**, 123524

[10] R. R. Das, D. M. Kim, S. H. Baek, C. B. Eom, F. Zavaliche, S. Y. Yang, R. Ramesh, Y. B. Chen, X. Q. Pan, X. Ke, M. S. Rzchowski and S. K. Streiffer, Appl. Phys. Lett., 2006, **88**, 242904

[11] H. W. Jang, D. Ortiz, S.-H. Baek, C. M. Folkman, R. R. Das, P. Shafer, Y. Chen, C. T. Nelson, X. Pan, R. Ramesh and C.-B. Eom, Adv. Mater., 2009, **21**, 817

[12] C. Wang, K.-j. Jin, Z.-t. Xu, L. Wang, C. Ge, H.-b. Lu, H.-z. Guo, M. He and G.-z. Yang, Appl. Phys. Lett., 2011, **98**, 192901

[13] A. Rana, H. Lu, K. Bogle, Q. Zhang, R. Vasudevan, V. Thakare, A. Gruverman, S. Ogale and V. Nagarajan, Adv. Funct. Mater., 2014, **24**, 3962

[14] D. Y. Zhang, W. X. Yu, D. L. Hao, L. L. Li, H. Liu and Z. W. Lu, J. Mater. Chem, 2012, **22**, 17328

[15] C. J. Brinker, and G.W. Scherer, Sol-Gel Science: The Physics and Chemistry of Sol-Gel Processing, Academic Press, Boston, 1990

[16] X. D. Qi, J. Dho, R. Tomov, M. G. Blamire and J. L. MacManus-Driscoll, Appl. Phys. Lett., 2005, **86**, 062903

[17] F. Tyholdt, S. Jorgensen, H. Fjellvag and A. E. Gunnaes, J. Mater. Res., 2005, **20**, 2127

[18] S. Iakovlev, C. H. Solterbeck, M. Kuhnke and M. Es-Souni, J. Appl. Phys., 2005, **97**, 094901

[19] M. Valant, A. K. Axelsson and N. Alford, Chem. Mater., 2007, **19**, 5431

[20] M. Ohyama, H. Kozuka and T. Yoko, J. Am. Ceram. Soc., 1998, **81**, 1622

[21] J. G. Wan, X. W. Wang, Y. J. Wu, M. Zeng, Y. Wang, H. Jiang, W. Q. Zhou, G. H. Wang and J. M. Liu, Appl. Phys. Lett., 2005, **86**, 122501

[22] L.G.Hubert-Pfalzgraf, J. Mater. Chem., 2004, **14**, 3113

[23] A.C.Jones, J. Mater. Chem., 2002, **12**, 2576

[24] S. Y. Yang, F. Zavaliche, L. Mohaddes-Ardabili, V. Vaithyanathan, D. G. Schlom, Y. J. Lee, Y. H. Chu, M. P. Cruz, Q. Zhan, T. Zhao and R. Ramesh, Appl., Phys, Lett., 2005, **87**, 102903

[25] R. Ueno, S. Okaura, H. Funakubo and K. Saito, Jpn. J. Appl. Phys. Part 2 - Lett. Express Lett., 2005, **44**, L1231

[26] S. K. Singh, R. Ueno, H. Funakubo, H. Uchida, S. Koda and H. Ishiwara, Jpn. J. Appl. Phys. Part 1, 2005, **44**, 8525

[27] S. K. Singh and H. Ishiwara, Jpn. J. Appl. Phys. Part 2 - Lett. Express Lett., 2005,**44**, L734

[28] Y. Nakamura, S. Nakashima and M. Okuyama, J. Appl. Phys., 2009, **105**, 061616

[29] S. K. Singh, Y. K. Kim, H. Funakubo and H. Ishiwara, Appl. Phys. Lett., 2006, **88**, 162904

[30] F. Tyholdt, H. Fjellvag, A. E. Gunnaes and A. Olsen, J. Appl. Phys., 2007, **102**, 074108

[31] X. Tang, X. Zhu, J. Dai and Y. Sun, Acta Mater., 2013, **61**, 1739

[32] Y. Nakamura, K.-Y. Yun, S. Nakashima and M. Okuyama, Integr. Ferroelectr., 2007, **95**, 226; Y. Nakamura, S. Nakashima and M. Okuyama, Jpn. J. Appl. Phys., 2008, **47**, 7250

[33] R.W.Schwartz, Chem. Mater., 1997, **9**, 2325

[34] X. Z. Wang, H. R. Liu and B. W. Yan, J. Euro. Ceram. Soc., 2009, **29**, 1183

[35] D. M. Tahan, A. Safari and L. C. Klein, J. Am. Ceram. Soc., 1996, **79**, 1593

[36] Q. Zhang and R. W. Whatmore, J. Phys. D-Appl. Phys., 2001, **34**, 2296

[37] Q. Zhang, V.Nagarajan, O. Standard, J. Appl. Phys., 2014, **116**, 066810

[38] G. N. Laura Fe and D. J. Wouters, J. Sol-Gel Sci. Technol., 2000, **19**, 149

[39] G. Socrates, ed., Infrared and Raman Characteristic Group Frequencies: Tables and Charts, Wiley, New York, 3rd edn., 2004

[40] G. D.Robertson, D.M.Mason and W.H.Corcoran, J. Phys. Chem., 1955, **59**, 683

[41] J. M. Bothwell, S. W. Krabbe and R. S. Mohan, Chem. Soc. Rev., 2011, **40**, 4649

[42] C. R. Gong, D. R. Chen, X. L. Jiao and Q. L. Wang, J. Mater. Chem., 2002, **12**, 1844

[43] S. Aggarwal, S. Madhukar, B. Nagaraj, I. G. Jenkins, R. Ramesh, L. Boyer and J. T. Evans, Appl. Phys. Lett., 1999, **75**, 716

[44] A. Tsurumaki, H. Yamada and A. Sawa, Adv. Funct. Mater., 2012, **22**, 1040

[45] F.Zavaliche, S.Y.Yang, T.Zhao, Y.H.Chu, M.P.Cruz, C.B.Eom and R.Ramesh, Phase Transit., 2006, **79**, 991

[46] Y.Ishibashi and H. Orihara, Integr. Ferroelectr., 1995, **9**, 57

[47] T. Tsurumi, S.M. Nam, Y. B. Kil and A. Wada, Asian Ceramic Science for Electronics. 2002, 123

[48] J.F.Scott, Integr. Ferroelectr., 1996, **12**, 71

Tables

Table 1. Composition of starting materials of precursor solutions

	Precursor Concentration	Bi(NO$_3$)$_3$·5H$_2$O	Fe(NO$_3$)$_3$·9H$_2$O	2-MOE	Acetic anhydride
Precursor A	**0.25 M**	0.015 mol	0.015 mol	0.75 mol (60 ml)	-
Precursor B	**0.25 M**	0.015 mol	0.015 mol	0.50 mol (40 ml)	0.21 mol (20 ml)
Precursor B	**0.35 M**	0.015 mol	0.015 mol	0.29 mol (23 ml)	0.21 mol (20 ml)
Precursor B	**0.45 M**	0.015 mol	0.015 mol	0.16 mol (13 ml)	0.21 mol (20 ml)

Table 2. Summary of FTIR spectra of 2-MOE, precursor A before and after heating for 75s

	Wavenumber (cm^{-1})			
Functional groups	**C-O** in R-O-R`	**C-O** in -CH$_2$-CH$_2$-OH	**C-O** in general	**O-H** in -CH$_2$-OH
2-MOE	1121	1061	1017	963
Precursor A Starting material	1119	1060	1016	963
Precursor A After heating for 75 s	1087 1111	-	1009 1031	-

Table 3. Summary of FTIR spectra of precursor B before and after heating for 90s

(a) C-O stretch bond

	Wavenumber (cm^{-1})		
Functional groups	**C-O** in R-O-R`	**C-O** in -CH$_2$-CH$_2$-OH	**C-O** in general
Precursor B Starting material	1125 1100	1052	1016
Precursor B After heating for 90 s	1126 1090	-	1006 1046

(b) C=O stretch bond

	Wavenumber (cm^{-1})	
Functional group	**C=O** in RCOOR`	**C=O** in CH$_3$COOH
Precursor B Starting material	1739	1722
Precursor B After heating for 90 s	1739	1709

Table 4 Summary of the reaction sequence of the precursor preparation and gelation processes using Precursor B

M = Bi^{3+} or Fe^{3+}; R = $CH_3OCH_2CH_2–$ or $CH_3CO–$

Eqn	Description	Chemical Reaction
2	Reaction of acetic anhydride with water (the latter from water of crystallization of the starting metal nitrates)	$(CH_3CO)_2O + H_2O \rightarrow 2CH_3COOH$
3	Esterification between acetic anhydride and 2MOE solvent	$(CH_3CO)_2O + CH_3OCH_2CH_2OH$ $\rightarrow CH_3COOH + CH_3OCH_2CH_2OCOCH_3$
1	Reaction of metal nitrate with 2-MOE solvent	$M(NO_3)_3 + 3[CH_3OCH_2CH_2OH]$ $\leftrightarrow M(OCH_2CH_2OCH_3)_3 + 3HNO_3$
4	Reaction of metal nitrate with 2-MOE solvent and acetic acid	$M(NO_3)_3 + x[CH_3OCH_2CH_2OH] + (3-x)CH_3COOH$ $\leftrightarrow M(OCH_2CH_2OCH_3)_x (OOCCH_3)_{3-x} + 3HNO_3$ (where $x \leq 3$)
7	Condensation reaction of reaction product from Eqn 1 or 4	$n[M(OR)_3]$ $\rightarrow M(OR)_2–[OM(OR)]_{n-2}–OM(OR)_2 + (n-1)ROR$

Table 5.Summary of effect of heating conditions on film microstructure

(i) Effect of temperature

Precursor Concentration	**Heating temperature**					
	R.T.	**50°C**	**60°C**	**70°C**	**80°C**	**90°C**
0.25 M	Precipitate (metal salts)	Precipitate (metal salts)	Precipitate (metal salts)	Gel	Gel	Gel
0. 35 M	Precipitate (metal salts)	Precipitate (metal salts)	Precipitate (metal salts)	Gel	Gel	Gel
0.45 M	Precipitate (metal salts)	Precipitate (metal salts)	Precipitate (metal salts)	Gel	Gel	Gel

(ii) Effect of heating duration

Precursor Concentration	**Heating duration**			
	1 min	**3 mins**	**10 mins**	**20 mins**
0.25 M	Precipitate (metal salts)	Precipitate (metal salts)	Gel	Gel
0. 35 M	Precipitate (metal salts)	Precipitate (metal salts)	Gel	Gel
0.45 M	Precipitate (metal salts)	Precipitate (metal salts)	Gel	Gel

Figures

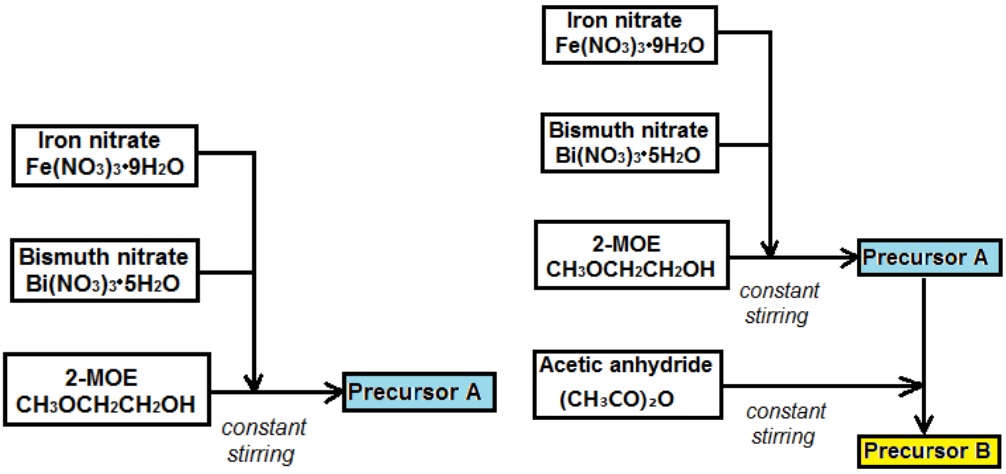

Fig. 1. Flow chart of precursor preparation

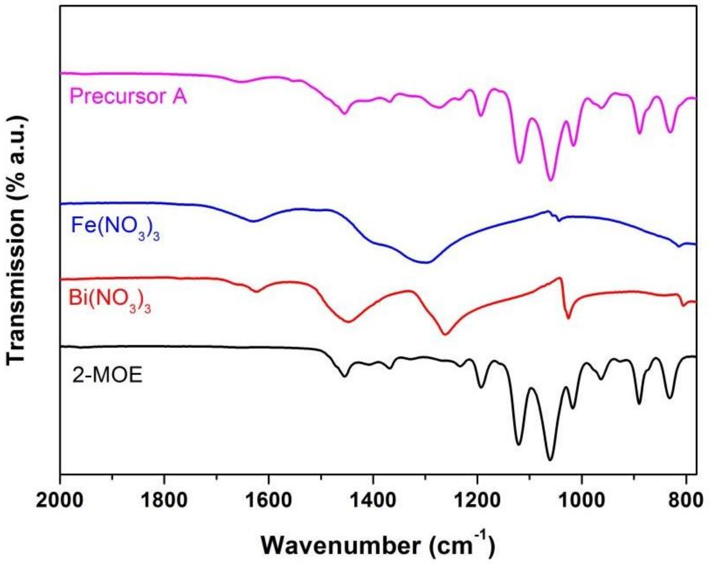

Fig. 2. FTIR spectra of raw materials and as-prepared Precursor A

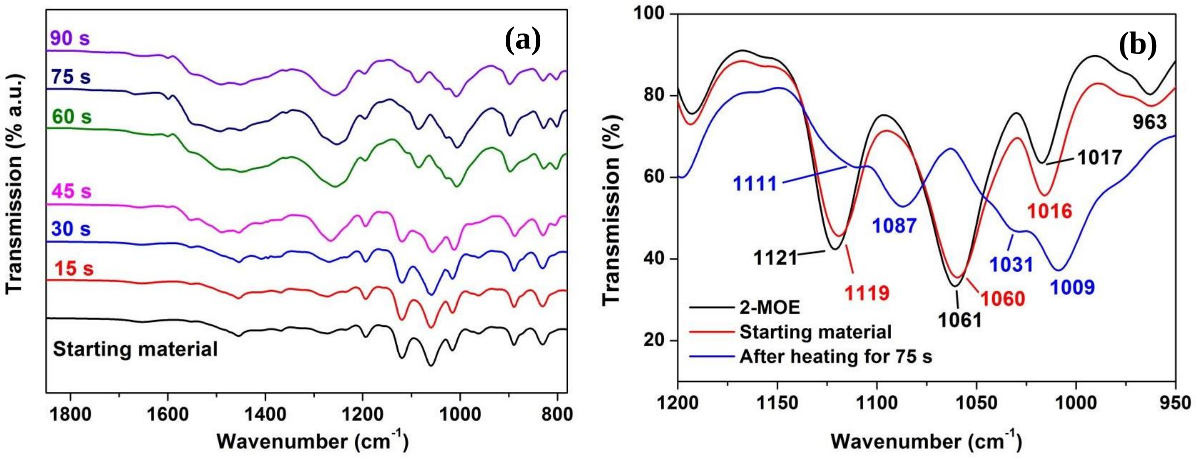

Fig. 3. (a) FTIR spectra of Precursor A starting material before heating and after heating for various durations at 90°C, 1850-780 cm^{-1}; (b) FTIR spectra of 2-MOE and Precursor A starting material before heating and after heating at 90°C for 75s, 1200-950 cm^{-1}

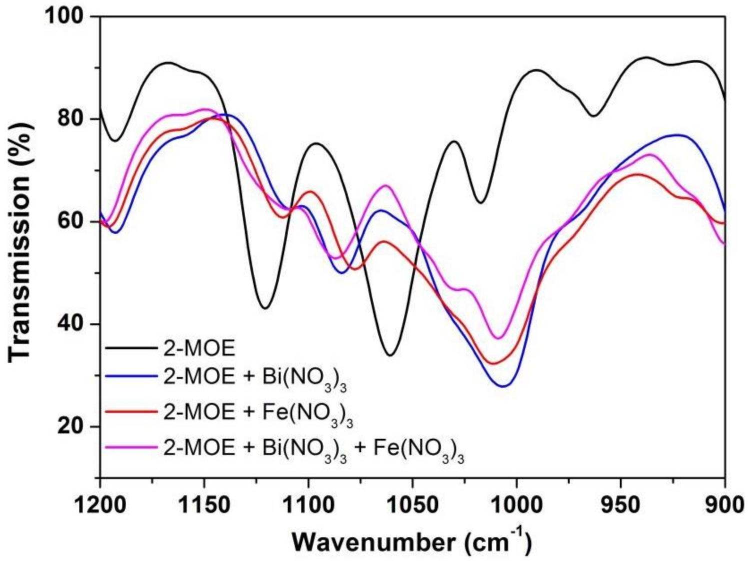

Fig. 4. FTIR spectra of 2-MOE and metal nitrates in 2-MOE precursor after heating at 90°C for 75s

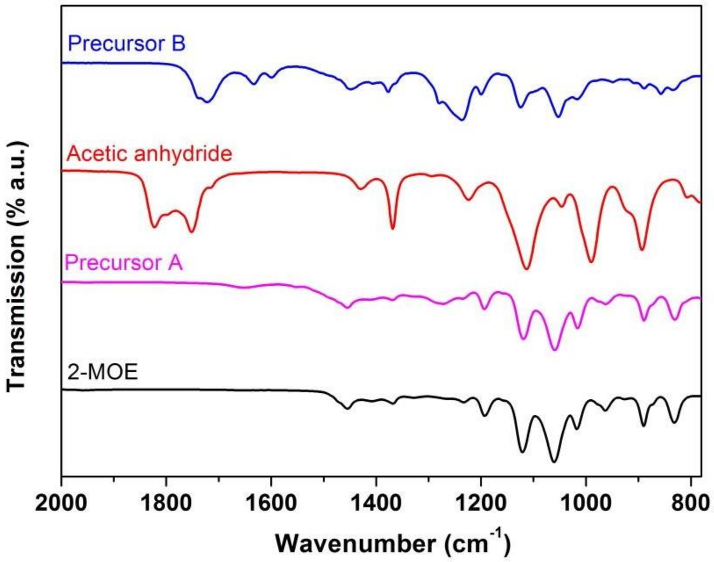

Fig. 5. FTIR spectra of raw materials and as-prepared precursors

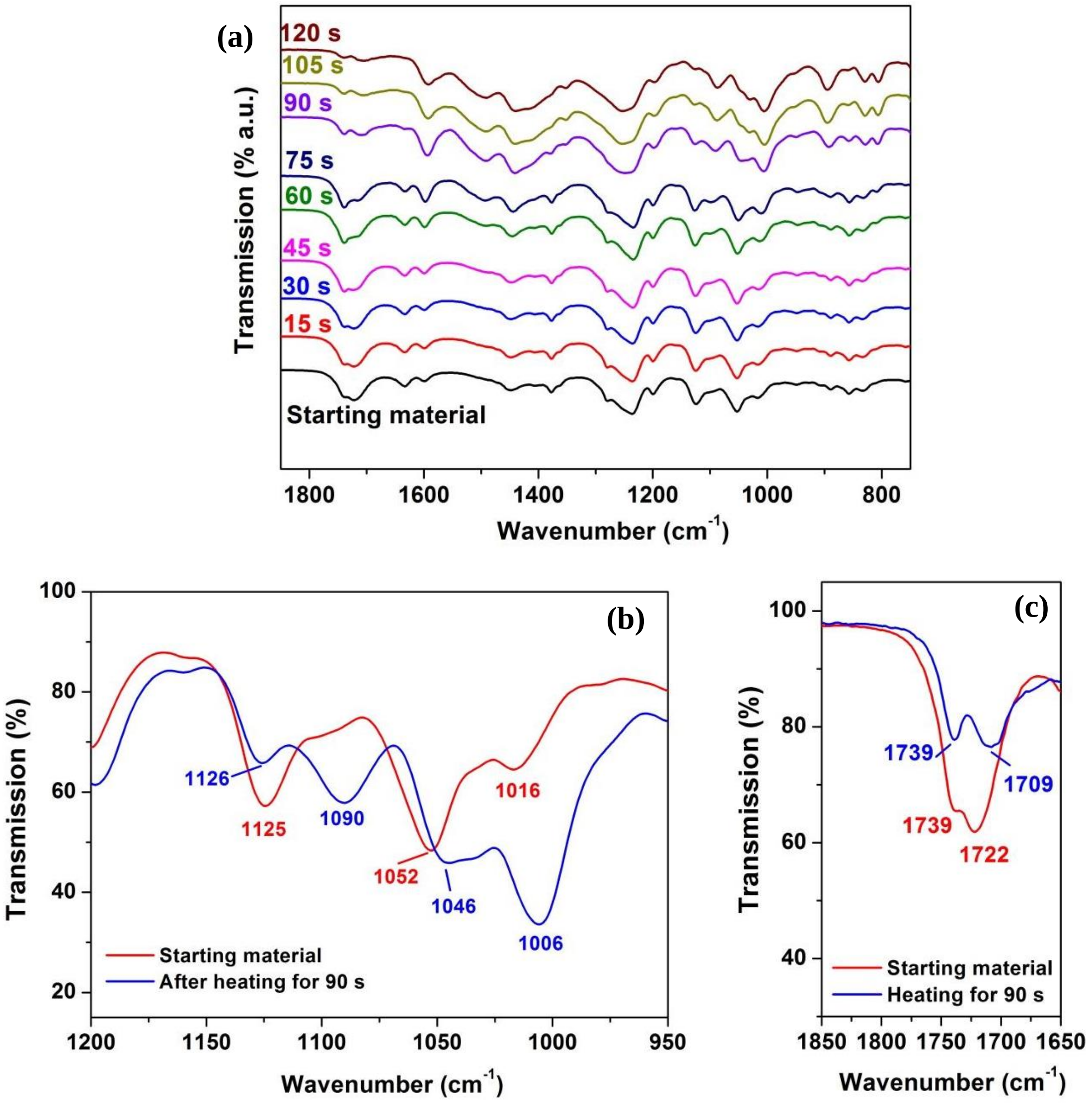

Fig. 6. (a) FTIR spectra of Precursor B starting material before and after heating for various durations at 90°C, 1850-780 cm^{-1}; (b) FTIR spectra of Precursor B starting material before heating and after heating at 90°C for 90s, 1200-950 cm^{-1}; (c) FTIR spectra of Precursor B starting material before heating and after heating at 90°C for 90s, 1850-1650 cm^{-1}

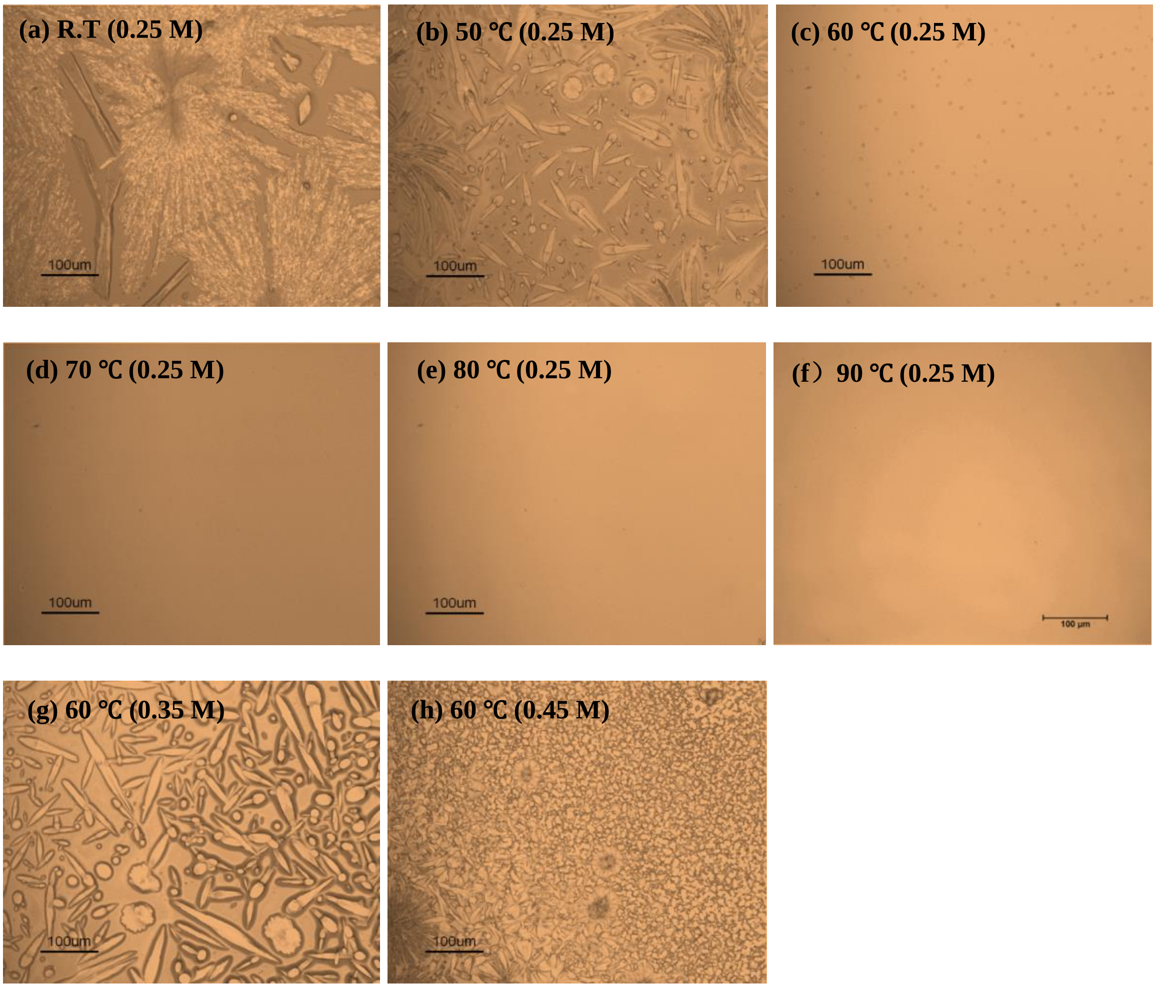

Fig. 7. Microscopic structures of as-deposited thin films after heating at various temperatures ((a) No heat treatment; (b) 50°C;(c)(g)(h) 60°C; (d) 70°C; (e) 80°C; (f) 90°C) for 10 minutes, followed by drying at room temperature in an open ambient air for 12 hours (Thin films prepared by 0.25 M (a)-(f), 0.35 M (g) and 0.45 M(h) precursors)

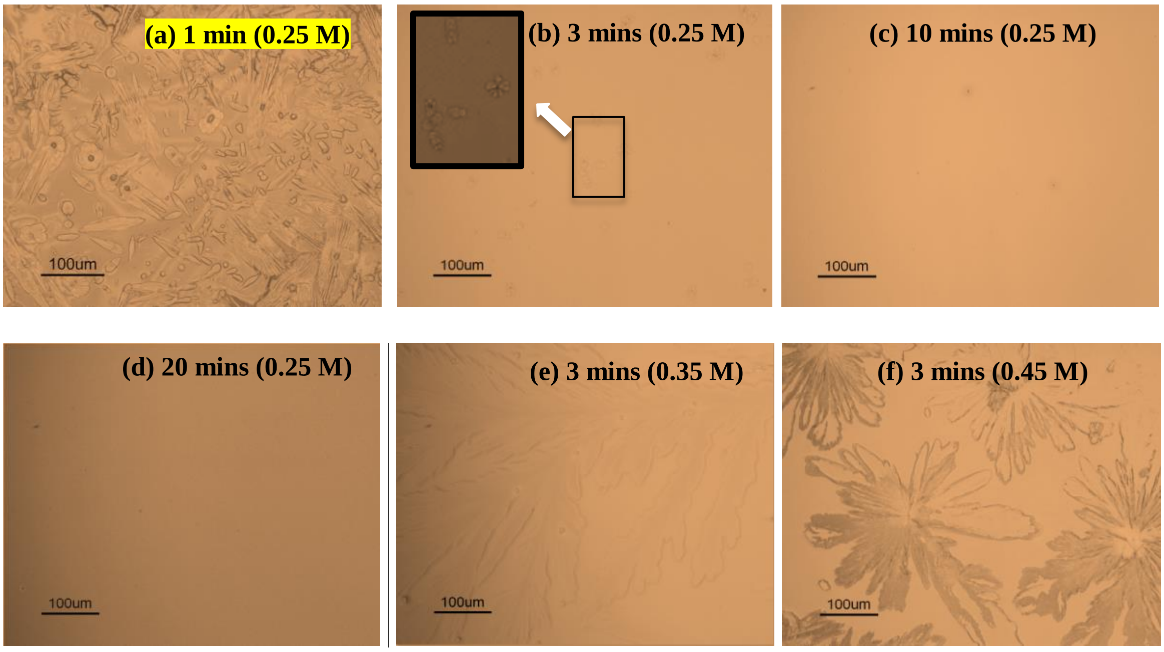

Fig. 8. Microscopic structures of as-deposited thin films after heating at 70°C for various durations ((a) 1 minute; (b)(e)(f) 3 minutes; (c) 10 minutes; (d) 20 minutes), followed by drying at room temperature in an ambient air for 12 hours (Thin films prepared by 0.25 M(a)-(d), 0.35 M (e) and 0.45 M(f) precursors)

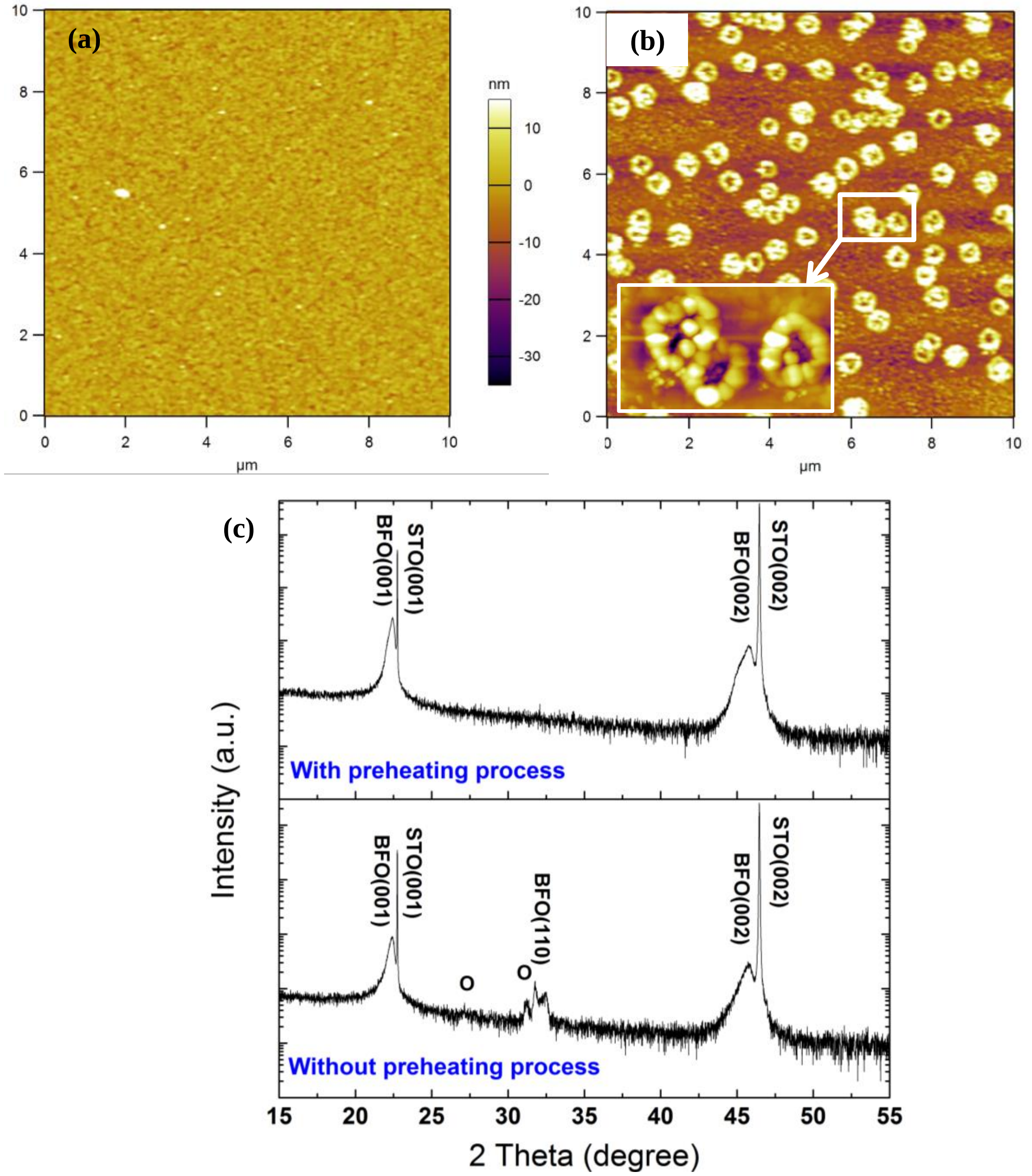

Fig. 9. AFM topographies (a)(b) and XRD patterns (c) of BFO /STO(001) thin films after heating at 650°C for 30 minutes in an oxygen atmosphere, using preheating(a) and no preheating(b) processes (O: bismuth rich phase)

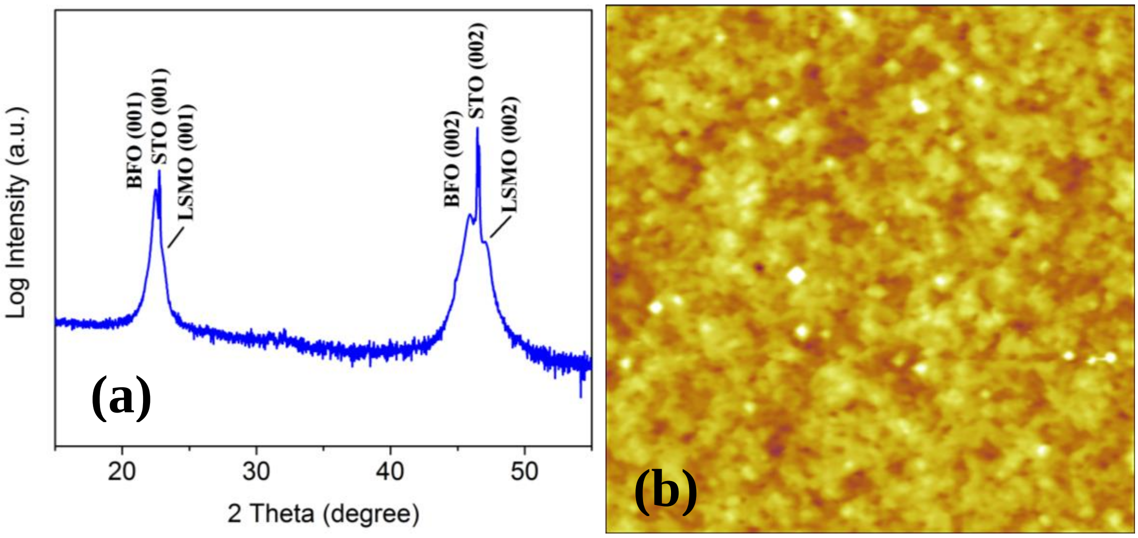

Fig. 10. (a) XRD pattern and (b) AFM topography image (5 μm × 5 μm) of (001) BFO/LSMO/STO thin film;

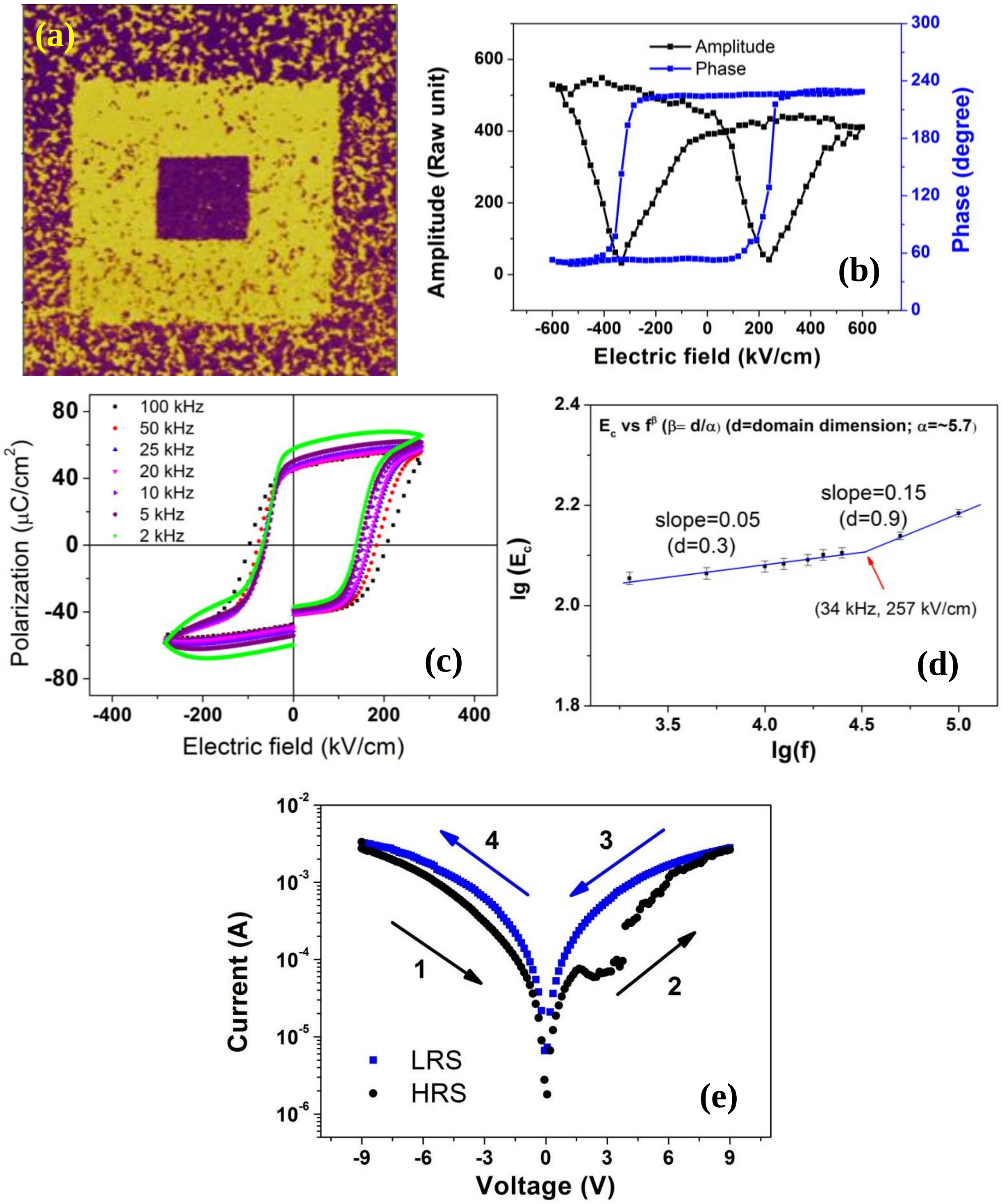

Fig. 11. (a) PFM phase image (5 μm × 5 μm) of a polarization pattern of BFO thin film after writing by DC bias with -9 V (3 μm × 3 μm) and +9 V (1 μm × 1 μm); (b) Local PFM phase and amplitude hysteresis loops of BFO thin films; (c) Ferroelectric polarization hysteresis loops of BFO thin films measured at 2 kHz-100 kHz; (d) The coercive field ($2E_c$) as a function of frequency; (e) I-V curve of BFO thin films. All measurements are taken at room temperature

The critical role of gelation is demonstrated in order to achieve epitaxial (001)-BFO thin films with robust room-temperature ferroelectric properties